Development of high vorticity structures in incompressible 3D Euler equations

D.S. Agafontsev[1,2], E.A. Kuznetsov[2,3,4] and A.A. Mailybaev[5,6]

[1] *P. P. Shirshov Institute of Oceanology,*

36 Nakhimovsky prosp., 117218 Moscow, Russia

[2] *Novosibirsk State University, 2 Pirogova, 630090 Novosibirsk, Russia*

[3] *P.N. Lebedev Physical Institute, 53 Leninsky Ave., 119991 Moscow, Russia*

[4] *L.D. Landau Institute for Theoretical Physics,*

2 Kosygin str., 119334 Moscow, Russia

[5] *Instituto Nacional de Matemática Pura e Aplicada – IMPA, Rio de Janeiro, Brazil*

[6] *Institute of Mechanics, Lomonosov Moscow State University, Russia*

We perform the systematic numerical study of high vorticity structures that develop in the 3D incompressible Euler equations from generic large-scale initial conditions. We observe that a multitude of high vorticity structures appear in the form of thin vorticity sheets (pancakes). Our analysis reveals the self-similarity of the pancakes evolution, which is governed by two different exponents e^{-t/T_ℓ} and e^{t/T_ω} describing compression in the transverse direction and the vorticity growth respectively, with the universal ratio $T_\ell/T_\omega \approx 2/3$. We relate development of these structures to the gradual formation of the Kolmogorov energy spectrum $E_k \propto k^{-5/3}$, which we observe in a fully inviscid system. With the spectral analysis we demonstrate that the energy transfer to small scales is performed through the pancake structures, which accumulate in the Kolmogorov interval of scales and evolve according to the scaling law $\omega_{\max} \propto \ell^{-2/3}$ for the local vorticity maximums $\omega_{\max}$ and the transverse pancake scales ℓ.

I. INTRODUCTION

The problem of whether incompressible 3D Euler equations develop a singularity in finite time (usually termed as blowup or collapse) from smooth initial data of finite energy is one of the most long-standing open questions in fluid dynamics and applied mathematics [1–5]. In

physics, formation of a collapse is considered as the most effective mechanism enhancing the energy dissipation of regular motion. For example, dissipation of oceanic surface waves takes significantly less time than its estimate due to viscosity [6–8]. The difference is attributed to formation of white caps on wave crests and subsequent breaking of waves, which is the manifestation of collapse for surface waves. For developed hydrodynamic turbulence, this process is connected with the energy transfer from large (forced) scales to small (viscous) scales, where the energy eventually dissipates. In the Kolmogorov-Obukhov theory [9, 10], the velocity fluctuations δv at intermediate spatial scales ℓ obey the power-law $\langle |\delta v| \rangle \propto \varepsilon^{1/3} \ell^{1/3}$, where ε is the mean energy flux from large to small scales. This formula can be easily obtained from the dimensional analysis, see e.g. [11, 12]. According to the same dimensional arguments, the fluctuations of vorticity field $\boldsymbol{\omega} = \mathrm{rot}\, \mathbf{v}$ diverge at small scales $\ell \to 0$ as $\langle |\delta \omega| \rangle \propto \varepsilon^{1/3} \ell^{-2/3}$, while the time of the energy transfer from the energy-contained scale L to the viscous ones is finite and estimated as $T \sim L^{2/3} \varepsilon^{-1/3}$. Thus, formation of the Kolmogorov spectrum may be regarded to collapses of vorticity field; such mechanism can be observed in simplified (shell) models of turbulence [13, 14]. However, finite-time singularities are not necessary for the Kolmogorov turbulent spectra, since in case of the finite Reynolds numbers the exponential growth of vorticity is sufficient for energy to reach viscous scales in finite time [15]. See also [16, 17] for numerical studies on early stages of turbulent spectra formation.

There are several blowup and no-blowup criteria for the inviscid flows, which are useful both in analytical studies and numerical simulations. The widely used criterion is due to the Beale–Kato–Majda theorem [18], which states that the time integral of maximum vorticity must explode at a singular point. Several criteria, which also use the direction of vorticity, are developed by Constantin *et al.* [19], Deng *et al.* [20, 21] and Chae [22]. See also [23–25] for other regularity criteria. The blowup scenario based on the vortex lines breaking (or overturning) was analyzed in [26] in the framework of the integrable incompressible hydrodynamic model with the Hamiltonian $\int |\omega| d\mathbf{r}$ and the same symplectic operator [27] as for the 3D Euler equations (such unusual Hamiltonian can be obtained from the 3D Euler equations in the so-called local induction approximation). Formation of a singularity in the framework of renormalization group formalism was discussed in [28–31].

Possible formation of a singularity in incompressible 3D Euler equations has been extensively studied in the past decades with direct numerical simulations, which mainly refer to

the flow in a box with periodic boundary conditions. Below we provide a short review of these numerical results; see also a brief but extensive account in [32], as well as [33, 34] for the studies of blowup triggered by the boundary.

In 1992, Brachet et $al.$ [35] using spectral methods studied periodic flows with random initial conditions on 256^3 grids and also the Taylor–Green vortex on 864^3 grids, and found the energy spectrum well-approximated as $E_k(t) = ck^{-n(t)}e^{-2\delta(t)k}$. The exponent $\delta(t)$ clearly demonstrated the exponential decay with time, $\delta(t) \propto e^{-t/T}$. Maximum of vorticity was growing almost exponentially in time with the total increase by the factor of 6 for both initial conditions. The regions of high vorticity represented pancake-like structures in physical space, which were compressed in one direction while their sizes in other two directions did not change considerably. Such tendency towards the vortex sheets leads to depletion of nonlinearity and prevents the formation of a finite-time singularity, see the related discussion in [36–38]. Thus, further numerical studies were mainly focused on specific initial conditions providing enhanced vorticity growth [38], e.g., antiparallel or orthogonal vortices. Initial conditions were usually chosen to be symmetric, as this required less computational resources.

In 1993, Kerr [39] analyzed the interaction of two perturbed antiparallel vortex tubes on grids of up to $512 \times 256 \times 128$ using the Chebyshev method. The results were interpreted in favor of the blowup, $\max|\boldsymbol{\omega}| \sim (t_0 - t)^{-1}$, with an increase of the vorticity maximum by the factor of 24. In the subsequent publication [40], the two characteristic length scales of the singularity were identified as $\rho \sim (t_0 - t)$ and $R \sim (t_0 - t)^{1/2}$. However, recent numerical simulations performed by Hou and Li [24, 41] with the pseudo-spectral method on the $1536 \times 1024 \times 3072$ grid questioned the blowup behavior for these initial conditions. The solution was extended beyond the earlier estimated blowup time, showing that the maximum vorticity evolution is slower than doubly exponential. Later the analysis was reconsidered by Bustamante and Kerr [42], suggesting the hypothesis of the vorticity growth as $\max|\boldsymbol{\omega}| \sim (t_0 - t)^{-\gamma}$ for $\gamma > 1$, and then by Kerr [43] concluding with the double-exponential growth.

In 1998, Grauer et $al.$ [44] used the adaptive mesh refinement technique claimed to be equivalent to non-adaptive 2048^3 grids. The authors achieved maximum vorticity increase of about 10 times and interpreted their results in favor of the blowup hypothesis, $\max|\boldsymbol{\omega}| \sim (t_0 - t)^{-1}$. Similar conclusions were drawn in 2012 by Orlandi et $al.$ [45] for two colliding

Lamb dipoles on grids up to 1536^3. However, in both cases [44] and [45] the initial conditions had a singularity of vorticity derivatives.

Several studies considered the Pelz–Kida initial flow of high symmetry with the indication of blowup behavior reported in earlier works [46–48]. In 2008, Grafke *et al.* [49] performed comparison of different spectral and real-space numerical methods with the Pelz–Kida like initial flow. The authors achieved the increase of maximum vorticity by about 2.5 times for 512^3 grids and about 3.5 times for 1024^3 grids before the methods started to diverge noticeably. Then the adaptive mesh refinement simulations were carried out with the effective resolution of 4096^3 and vorticity maximum increase of about 6 times. These results, also confirmed by Hou and Li [50], demonstrated no tendency toward blowup at the times predicted earlier. It was also noted that the vorticity increased exponentially with time on the Lagrangian trajectory, which ended at the maximum vorticity point at the end of the simulations.

In the present paper, we analyze numerically the 3D Euler equations for rather generic large scale initial conditions in a periodic box, i.e., focusing on typical development of vorticity in inviscid incompressible flows. For numerical simulations, we use the pseudo-spectral method on adaptive rectangular grid. Our goal is the systematic study of high vorticity structures, including the maximum vorticity region and other local phenomena. We identify these structures by looking at local maximums of the vorticity modulus. We show that a multitude of high vorticity structures appear and have the form of pancakes, i.e., thin vorticity sheets compressing exponentially in time in a self-similar way for the pancake transverse direction. Unlike the pancake model proposed in [35], this self-similar dependence is governed by two different exponents for the pancake compression and the vorticity growth; we suggest how the pancake model [35] can be modified to capture the observed behavior. Due to the exponential vorticity growth, no tendency toward the blowup is observed.

Our main result is the demonstration of close relation between the collective evolution of pancake vorticity structures and the formation of Kolmogorov turbulent spectra. Our simulations show that the Kolmogorov energy spectrum starts to form in the fully inviscid system, where numerical error is kept very small (the flow is not affected by small-scale finite grid effects as opposed to [51]). With the analysis of local maximums we argue that the Kolmogorov spectrum is attributed to the pancake structures, which accumulate in the same interval of scales and evolve according to the scaling law for the local vorticity

maximums as $\omega_{\max} \propto \ell^{-2/3}$, where ℓ is the pancake thickness. Though our conclusions are limited by the numerical resources that allow the Kolmogorov interval of about one decade, our results provide a new insight on the development of high vorticity structures in relation with the turbulent spectra, and indicate the importance of further study in this direction. In addition to these results, in our next paper we will present numerical simulations performed in the vortex lines representation variables. The vortex lines representation developed by Kuznetsov and Ruban [26, 52, 53] describes the flow from the point of view of the moving vortex lines, which are compressible. This representation helps in understanding some of the numerical observations presented in the current paper, including the scaling law $\omega_{\max} \propto \ell^{-2/3}$ between the local vorticity maximums $\omega_{\max}$ and the transverse pancake scales ℓ.

The paper is organized as follows. Section II describes the numerical method. In Section III we study the pancake structure near the global vorticity maximum, while in Section IV we focus on the statistics of local maximums. Section V discusses the numerical observation of the Kolmogorov spectrum and its relation to extreme vorticity structures. The final Section VI contains conclusions. The Appendices A and B contain the initial conditions and the results of the second simulation.

II. NUMERICAL METHOD

The Euler equations describing dynamics of ideal incompressible fluid of unit density in three-dimensional space are

$$\frac{\partial \mathbf{v}}{\partial t} + (\mathbf{v} \cdot \nabla)\mathbf{v} = -\nabla p, \quad \operatorname{div} \mathbf{v} = 0, \tag{1}$$

where the velocity field $\mathbf{v} = (v_x, v_y, v_z)$ and pressure p are smooth functions of space coordinates $\mathbf{r} = (x, y, z)$ and time t. We consider solutions of Eq. (1) in the box $\mathbf{r} \in [-\pi, \pi]^3$ with periodic boundary conditions. For numerical simulations, we use the formulation of Euler equations in terms of vorticity (also known as Helmholtz's vorticity equations),

$$\frac{\partial \boldsymbol{\omega}}{\partial t} = \operatorname{rot}(\mathbf{v} \times \boldsymbol{\omega}), \quad \mathbf{v} = \operatorname{rot}^{-1}\boldsymbol{\omega}. \tag{2}$$

Assuming the vanishing average velocity $\int \mathbf{v} d^3\mathbf{r} = 0$, the inverse of the rotor operator in Eq. (2) is uniquely defined and has the form

$$\mathbf{v}(\mathbf{k}) = \frac{i\mathbf{k} \times \boldsymbol{\omega}(\mathbf{k})}{k^2} \quad \text{for} \quad k = \|\mathbf{k}\| \neq 0; \quad \mathbf{v}(\mathbf{0}) = \mathbf{0}, \tag{3}$$
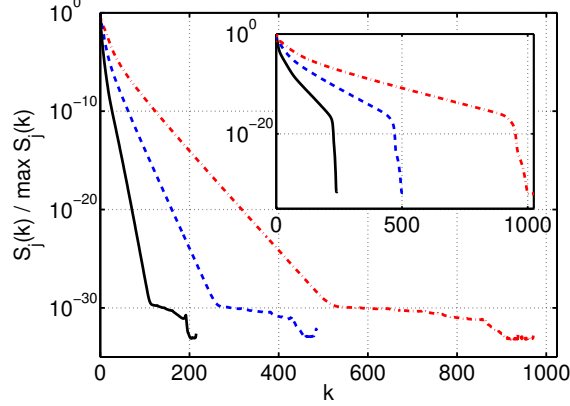
FIG. 1: *(Color on-line)* Normalized spectra of the vorticity field $S_j(k)/\max_k S_j(k)$ along the j-axis (x solid black, y dashed blue, z dash-dot red) for the initial data I_1 (see Eq. (6) and Tab. I in the Appendix A) at $t = 5$ and at the final time $t = 6.89$ (inset).

for the Fourier transformed velocity $\mathbf{v}(\mathbf{k})$ and vorticity $\boldsymbol{\omega}(\mathbf{k})$. The wavevector $\mathbf{k} = (k_x, k_y, k_z)$ has integer components for the periodic box, $\mathbf{r} \in [-\pi, \pi]^3$. Note that the transformation (3) automatically satisfies the incompressibility condition, $\mathbf{k} \cdot \mathbf{v}(\mathbf{k}) = 0$.

A.   Adaptive scheme and initial conditions

We solve the system (2) numerically using the pseudo-spectral method in the adaptive rectangular grid, which is uniform along each coordinate. The number of nodes N_x, N_y and N_z in each direction is adapted independently, as explained below. To avoid the so-called bottle-neck instability we perform the filtering in Fourier space with the cut-off function [41]

$$\rho(\mathbf{k}) = \exp\left(- 36\left[\left(\frac{k_x}{K_x}\right)^{36} + \left(\frac{k_y}{K_y}\right)^{36} + \left(\frac{k_z}{K_z}\right)^{36} \right]\right). \tag{4}$$

Here $K_j = N_j/2$ are the maximum wavenumbers along directions $j = x, y, z$, i.e., $k_j \in [-K_j, K_j]$. Function (4) cuts off approximately 20% of the spectrum at the edges of the spectral band in each direction. We use the fourth-order Runge–Kutta method with the adaptive time stepping, which is implemented according to the CFL stability criterion with the Courant number 0.5.

For optimal performance, we start simulations with the 128^3 grid, which is appropriate

for large-scale initial conditions. The adaptive scheme is controlled by the functions

$$S_j(k) = \int |\boldsymbol{\omega}(\mathbf{p})|^2 \delta(|p_j| - k)\, d^3\mathbf{p}, \quad j = x, y, z, \tag{5}$$

which describe the enstrophy spectrum along each axis. As shown in Fig. 1, these functions have breakpoints approximately at the level of $\sim 10^{-30}$, which corresponds to numerical noise. During the simulation, these breakpoints move to larger k reflecting the excitation of higher harmonics. We stop the simulation every time when one of the breakpoints reaches the value of $2K_j/3$ for the corresponding axis, and then continue with the refined grid which has increased number of points N_j along the axis j. The vorticity field is interpolated to the new grid using the Fourier interpolation procedure, which has an error comparable to round-off. The simulations carried out in this way are not affected by the aliasing errors. After the total number of nodes $N_x N_y N_z$ reaches 1024^3, we continue the simulation with the fixed grid and stop when any of the values $S_j(2K_j/3)$ reaches $10^{-13} \max_k S_j(k)$, see Fig. 1(inset).

We tested our simulations with smaller time steps, different harmonics filtering, including the standard 2/3 cut-off rule [41], and found negligible difference in the results. The simulations conserve the total energy $E = \frac{1}{2}\int |\mathbf{v}|^2\, d\mathbf{r}$ and helicity $\Omega = \int (\mathbf{v} \cdot \boldsymbol{\omega})\, d\mathbf{r}$ with a relative error smaller than 10^{-11}. We also compared our simulations performed with different limitations for the maximal total number of nodes, and found that the results perfectly converge. For instance, in the time interval $4.13 \leq t \leq 5.83$, where the simulations with $N_x N_y N_z \leq 512^3$ and $N_x N_y N_z \leq 1024^3$ run on different grids, the relative difference for the maximum vorticity is less than 10^{-3}. The main source of this difference is attributed to the fact that different nodes of the grids are used for approximating the maximum. Note that the high accuracy used in our simulations is crucial for the detailed analysis of extreme structures in the flow, which requires very accurate computation of higher-order derivatives near local maximums of the vorticity. For less accurate simulations, numerical errors in these regions increase and the simulation results become unsatisfactory for our purposes.

We consider initial conditions represented in the form of Fourier series

$$t = 0: \quad \boldsymbol{\omega}(\mathbf{r}) = \sum_{\mathbf{h}} [\mathbf{A_h} \cos(\mathbf{h} \cdot \mathbf{r}) + \mathbf{B_h} \sin(\mathbf{h} \cdot \mathbf{r})], \tag{6}$$

where $\mathbf{h} = (h_x, h_y, h_z)$ is a vector with integer components. Since $\operatorname{div} \boldsymbol{\omega} = 0$, the real vectors $\mathbf{A_h}$ and $\mathbf{B_h}$ must satisfy the orthogonality conditions, $\mathbf{h} \cdot \mathbf{A_h} = \mathbf{h} \cdot \mathbf{B_h} = 0$. We

fix the vectors $\mathbf{A}_{(0,0,1)} = (0,1,0)$ and $\mathbf{B}_{(0,0,1)} = (1,0,0)$, and choose the other coefficients as random numbers with zero mean and variance $\sigma_{\mathbf{h}}^2 \sim \exp(-|\mathbf{h}|^2)$. Thus, the initial conditions represent the large-scale vorticity field given by the shear flow (degenerate ABC flow)

$$\omega_x = \sin(z), \quad \omega_y = \cos(z), \quad \omega_z = 0, \tag{7}$$

which is the exact stationary solution of the 3D Euler equations, with a random perturbation.

A number of initial conditions were tested with the purpose of choosing good candidates for the final high precision simulations. We selected the two initial conditions with better performance for the global vorticity maximum and relatively small number of excited harmonics, which are denoted as I_1 and I_2 and summarized in Tabs. I and II in the Appendix A along with some simulation information. We focus our analysis on the simulation for the initial condition I_1, which reaches the time $t = 6.89$ on the grid $486 \times 1024 \times 2048$. The different number of grid points for different directions results from the adaptive scheme, which resolves the anisotropy of vorticity in an optimal way. In the Sections below this simulation will be always assumed unless otherwise stated. The simulation results for the initial condition I_2 are summarized in the Appendix B.

B. Analysis of high vorticity structures

As we demonstrate in the next Sections, the regions of high vorticity are strongly anisotropic and develop in the form of pancake-like structures, which are thin in one direction and remain large in other two directions, Fig. 2(a). Conclusions of our paper rely significantly on the systematic identification of such structures, which is performed by searching for local maximums of the vorticity modulus $|\boldsymbol{\omega}(\mathbf{r})|$. The values of vorticity in the pancake are very sensitive to the distance from the pancake midplane, while the shifts along this plane have much smaller effects. Thus, searching for maximums by a simple comparison of neighboring grid points yields a large number (up to thousands) of "false" local maximums. For this reason, we developed a three-step numerical procedure for the identification of "true" local maximums.

At each grid point $\mathbf{r}_g$, we compute the gradient vector $\mathbf{g}(\mathbf{r}_g) = \nabla|\boldsymbol{\omega}|$ and the Hessian matrix $\mathbf{H}(\mathbf{r}_g) = [\partial^2 |\boldsymbol{\omega}|/\partial x_i \partial x_j]$ using the spectral method. A local maximum is characterized by the vanishing gradient vector and negative definite Hessian matrix, which has three
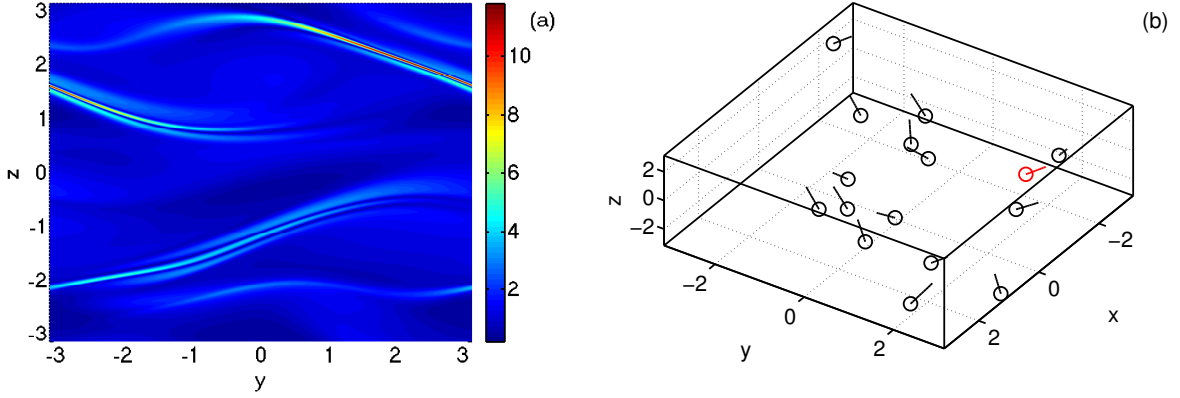
FIG. 2: *(Color on-line)* (a) Vorticity field $|\boldsymbol{\omega}|$ at fixed $x = x_0$ at the final time $t = 6.89$. Here x_0 is the x-coordinate of the global maximum. (b) Positions (circles) of local maximums of $|\boldsymbol{\omega}|$ and directions (lines) of the eigenvectors $\mathbf{w}_1$ normal to the pancake structures, at $t = 6.89$. Red color marks the global maximum.

negative eigenvalues $\lambda_1 < \lambda_2 < \lambda_3 < 0$ with the orthonormal eigenvectors $\mathbf{w}_1$, $\mathbf{w}_2$, $\mathbf{w}_3$. As we will demonstrate below for the local maximums of vorticity, $|\lambda_1| \gg |\lambda_2| \sim |\lambda_3|$ and the eigenvector $\mathbf{w}_1$ determines the perpendicular direction to the pancake midplane while the eigenvectors $\mathbf{w}_2$ and $\mathbf{w}_3$ lie in this plane. Assuming that the local maximum $\mathbf{r}_m$ lies near $\mathbf{r}_g$, the second-order approximation yields

$$\mathbf{r}_m \approx \mathbf{r}_g - \mathbf{g}(\mathbf{r}_g)\mathbf{H}^{-1}(\mathbf{r}_g). \tag{8}$$

As the first step in our procedure, we check every grid node $\mathbf{r}_g$ to satisfy the following two conditions simultaneously: Eq. (8) yields the point $\mathbf{r}_m$ lying in one of the adjacent grid cells, and the Hessian matrix $\mathbf{H}(\mathbf{r}_g)$ is negative definite. These conditions determine a cloud of grid points around each local maximum. So, as the second step, we select a single node in each cloud by choosing the node with the smallest distance $|\mathbf{r}_m - \mathbf{r}_g|$. At larger times some of the pancake structures contain several local maximums of vorticity. Some of these maximums form localized clusters, within which local maximums have close values of vorticity, almost the same eigenvectors $\mathbf{w}_1$, and lie approximately in the same plane almost perpendicular to the eigenvectors $\mathbf{w}_1$. Thus, such maximums represent close and similar oriented parts of the same pancake. In the third step we determine all such clusters of local maximums, and leave only one point with the largest value of vorticity from each cluster.

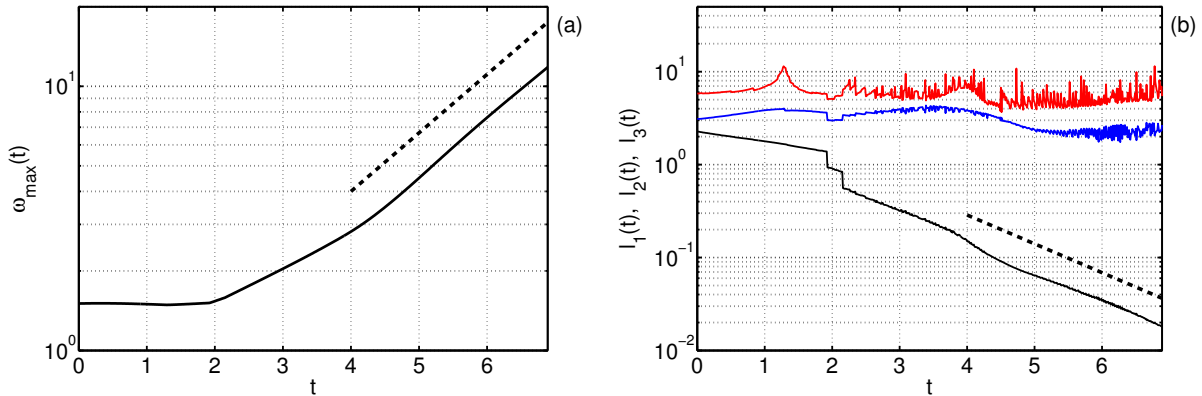We expect that the local maximums in the resulting set are associated with different

FIG. 3: *(Color on-line)* (a) Evolution of the global vorticity maximum (logarithmic vertical scale). The dashed line indicates the exponential slope $\propto e^{t/T_\omega}$ with characteristic time $T_\omega = 2$. (b) Evolution of characteristic spatial scales for the region of the global vorticity maximum, ℓ_1 (black), ℓ_2 (blue) and ℓ_3 (red). The dashed line indicates the exponential slope $\propto e^{-t/T_\ell}$ with characteristic time $T_\ell = 1.4$.

pancake structures or different (distant or differently oriented) parts of the same pancake, Fig. 2(b). The proposed method allows adequate selection of local maximums of vorticity, producing a little amount of false maximums. We compared its performance on significantly different grids, and found that the resulting sets of local maximums differ by no more than 10-15%.

III. EVOLUTION NEAR THE GLOBAL MAXIMUM OF VORTICITY

Numerical studies of singularities in the 3D incompressible Euler equations use the evolution of global vorticity maximum $\omega_{\mathrm{max}}(t) = \max |\boldsymbol{\omega}(\mathbf{r})|$ as one of the principal tests. According to the Beale–Kato–Majda theorem [18], unbounded increase of this maximum is necessary for the finite-time blowup. In this Section we consider the dynamics of $\omega_{\mathrm{max}}(t)$ and analyze the local geometry of the flow. The global vorticity maximum grows with time from the initial value $\omega_{\mathrm{max}}(0) \approx 1.5$ to 11.8 at the finial time of the simulation $t = 6.89$, Fig. 3(a). For $t > 4.5$, this growth is well-approximated by the exponential function $\omega_{\mathrm{max}}(t) \propto e^{t/T_\omega}$ with $T_\omega \approx 2$. Contrary to the vorticity, the velocity maximum $\max |\mathbf{v}(\mathbf{r})|$ does not change more than by 10% during the whole simulation.

Local geometry near the vorticity maximum can be studied using the Hessian matrix
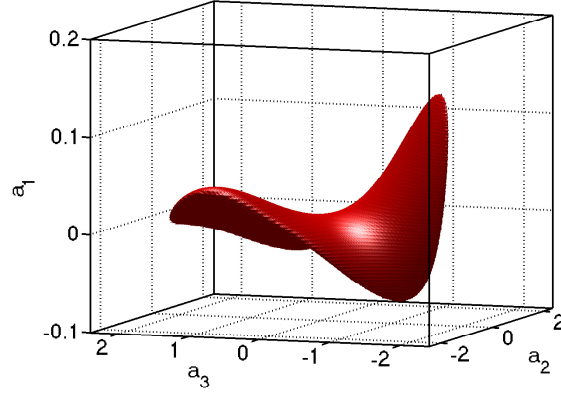
FIG. 4: *(Color on-line)* Isosurface of constant vorticity $|\boldsymbol{\omega}| = 0.8\,\omega_{\mathrm{max}}$ in the local coordinates (a_1, a_2, a_3) at the final time of the simulation, $t = 6.89$. Note much smaller vertical scale.

$\mathbf{H} = [\,\partial^2|\boldsymbol{\omega}|/\partial x_i \partial x_j\,]$ computed at the maximum point $\mathbf{r}_m$. This matrix has three negative eigenvalues $\lambda_1 < \lambda_2 < \lambda_3 < 0$ with the orthogonal eigenvectors $\mathbf{w}_1$, $\mathbf{w}_2$, $\mathbf{w}_3$. Considering the local orthonormal basis as $\mathbf{r} = \mathbf{r}_m + a_1\mathbf{w}_1 + a_2\mathbf{w}_2 + a_3\mathbf{w}_3$, the vorticity modulus can be described by the quadratic approximation

$$\frac{|\boldsymbol{\omega}(\mathbf{r})|}{\omega_{\mathrm{max}}} = 1 - \left(\frac{a_1}{\ell_1}\right)^2 - \left(\frac{a_2}{\ell_2}\right)^2 - \left(\frac{a_3}{\ell_3}\right)^2 + o(|\mathbf{r} - \mathbf{r}_m|^2), \quad \ell_j = \sqrt{\frac{2\omega_{\mathrm{max}}}{-\lambda_j}}. \tag{9}$$

The quantities ℓ_1, ℓ_2 and ℓ_3 determine the size of high vorticity region at fixed time, and their time evolution is shown in Fig. 3(b). Note that the discontinuities in this figure near $t = 2$ correspond to the change of global maximum among different local maximums, while the noise in determining ℓ_2 and ℓ_3 for larger times is the result of amplified numerical error due to the ill-conditioned Hessian matrix. The smallest size decreases exponentially in time, $\ell_1 \propto e^{-t/T_\ell}$ with $T_\ell \approx 1.4$ for $t > 4.5$, while ℓ_2 and ℓ_3 remain almost the same. At final time, we have $\ell_1/\ell_2 \sim \ell_1/\ell_3 \sim 10^{-2}$, which implies that the high-vorticity region represents a very thin pancake structure with the normal vector $\mathbf{w}_1$ and tangent vectors $\mathbf{w}_2$ and $\mathbf{w}_3$. This is confirmed in Fig. 4 (note the much smaller scale of the vertical axis) showing the numerically computed isosurface $|\boldsymbol{\omega}(\mathbf{r})| = 0.8\,\omega_{\mathrm{max}}$ in the coordinates (a_1, a_2, a_3).

Similar pancake structures were observed systematically in [35], where the singularity was analyzed by looking at the analyticity strip of the solution. This method relies on the evolution of the energy spectrum

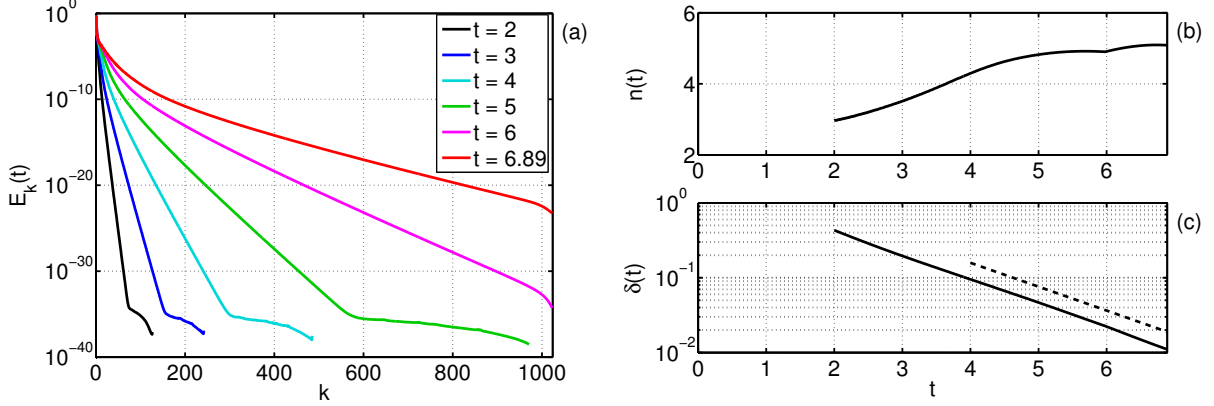$$E_k(t) = \frac{1}{2}\int |\mathbf{v}(\mathbf{k}, t)|^2 \, k^2 do, \tag{10}$$

FIG. 5: *(Color on-line)* (a) Energy spectrum $E_k(t)$ at different times. Figures (b) and (c) show the exponents $n(t)$ and $\delta(t)$ of the fit $E_k(t) \approx c(t)k^{-n(t)}e^{-2\delta(t)k}$. The dashed line in figure (c) indicates the exponential slope $\propto e^{-t/T_\delta}$ with characteristic time $T_\delta = 1.4$.

where o is the spherical angle. Numerically, we find $E_k(t)$ as a sum $\frac{1}{2} \sum |\mathbf{v}(\mathbf{k})|^2$ over all nodes in the spherical shell $k \leq |\mathbf{k}| < k + 1$. This procedure is simple and yields the result, which is very close to the direct computation of the integral in Eq. (10) with the interpolation of velocity Fourier components on the sphere of radius k.

For fixed time and sufficiently large wavenumbers, the energy spectrum decays with k exponentially, $E_k(t) \propto e^{-2\delta(t)k}$, possibly with an algebraic prefactor, until the level of $\sim 10^{-35}$ corresponding to numerical noise, Fig. 5(a). The exponent $\delta(t)$ can be associated with the width of analyticity strip for the solution extended to complex coordinates $\mathbf{r}$. In [35], the spectrum fitting $E_k(t) \approx c(t)k^{-n(t)}e^{-2\delta(t)k}$ was used and the function $\delta(t)$ showed the exponential decay $\delta(t) \propto e^{-t/T_\delta}$ at large times. Our simulations lead to the same conclusions with $T_\delta \approx 1.4$, Fig. 5(c). Note that $T_\delta \approx T_\ell$, where $T_\ell \approx 1.4$ describes the exponential decay of the pancake width (we estimate the absolute numerical accuracy for the time scales T_ω, T_ℓ and T_δ as ± 0.1). This relation is natural, since the analyticity strip must be determined by the most extreme event, i.e., by the thinnest part of a pancake at the point of maximum vorticity. Note that our results for the algebraic prefactor $n(t)$ differ from [35], where $n(t)$ approached -4 at late times, Fig. 5(b).

The following self-similar solution of the Euler equations was suggested in [35] for the description of the flow structure in a small neighborhood of the pancake,

$$v_1 = -\frac{a_1}{T}, \quad v_2 = \frac{a_2}{T}, \quad v_3 = f\left(a_1 e^{t/T}\right), \quad p = -\frac{a_1^2 + a_2^2}{2T^2}, \tag{11}$$

which is written in local coordinates (a_1, a_2, a_3) with the axis a_1 perpendicular to the pancake; v_j are components of the velocity, p is pressure and $f(a_1)$ is an arbitrary function. The model (11) leads to the exponential growth $\propto e^{t/T}$ of vorticity $\boldsymbol{\omega} = (\omega_1, \omega_2, \omega_3)$ as

$$\omega_1 = \omega_3 = 0, \quad \omega_2 = -e^{t/T} f'(a_1 e^{t/T}) \tag{12}$$

in the pancake, whose thickness decreases exponentially as $\propto e^{-t/T}$ with the same characteristic time T. However, our simulations demonstrate that the evolution of the pancake is governed by the two different exponents e^{t/T_ω}, $T_\omega \approx 2$, and e^{-t/T_ℓ}, $T_\ell \approx 1.4$, for the vorticity growth and the pancake compression, respectively. We propose that the flow near the pancake can be approximated as

$$v_1 = -\frac{a_1}{T_\ell}, \quad v_2 = \frac{a_2}{T_\ell}, \quad v_3 = e^{-\alpha t} f\left(a_1 e^{t/T_\ell}\right), \quad p = -\frac{a_1^2 + a_2^2}{2T_\ell^2}, \tag{13}$$

where $\alpha = 1/T_\ell - 1/T_\omega > 0$. The modified model (13) is not the solution of the Euler equations. However, it satisfies the incompressibility condition div $\mathbf{v} = 0$, yields the correct exponents for the maximum vorticity and the pancake thickness

$$\omega_1 = \omega_3 = 0, \quad \omega_2 = -e^{t/T_\omega} f'(a_1 e^{t/T_\ell}), \tag{14}$$

and after being substituted into the Euler equations (1), ensures the cancellation of the leading-order terms growing exponentially as $\propto e^{t/T_\omega}$, while the next-order terms (not canceled) decay as $\propto e^{-\alpha t}$.

Our pancake self-similarity hypothesis agrees well with the simulation results, see Fig. 6. Note that the vorticity vector near the pancake is mostly aligned with the eigenvector $\mathbf{w}_2$ (axis a_2), in agreement with the model given by Eqs. (13)-(14). One can expect that the pancake (13)-(14) contributes to the energy spectrum in the interval of wavenumbers $|k| \lesssim k_1$ with

$$k_1 = \frac{1}{\ell_1} \sim \frac{2\pi}{L}, \tag{15}$$

where $\ell_1 \propto e^{-t/T_\ell}$ is the characteristic scale along the axis a_1 in Eq. (9) and L estimates the oscillation period of vorticity components in Fig. 6(a); this relation can be deduced, e.g., by analogy with the Fourier transform of the function $\text{sech}(x/\ell_1)$. At final time, the numerical simulation yields $L \approx 0.13$ and $\ell_1 \approx 0.018$, which is in good agreement with relation (15).

It is worth noting that self-similar model (13)–(14) cannot be interpreted in the context of two-dimensional flow, since vorticity grows exponentially in time, while the vorticity vector
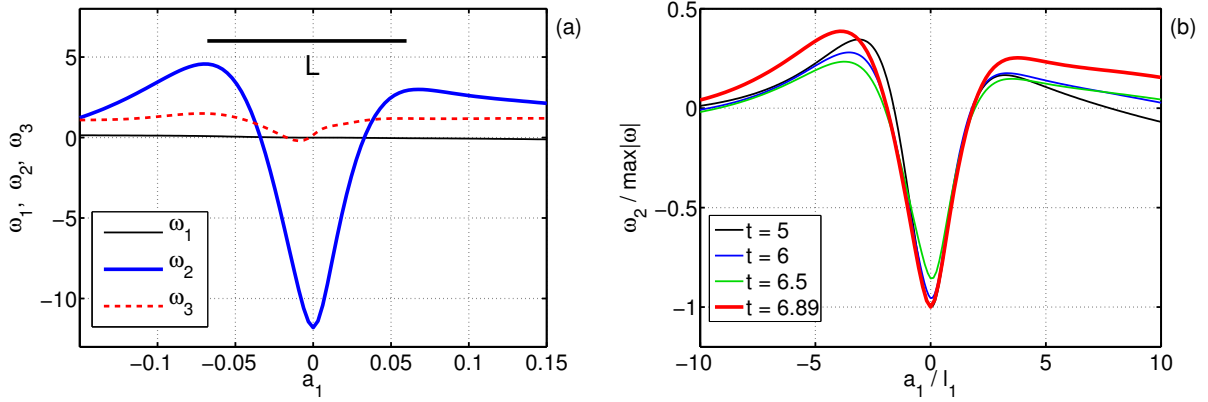
FIG. 6: *(Color on-line)* (a) Components of the vorticity vector $\boldsymbol{\omega} = \omega_1 \mathbf{w}_1 + \omega_2 \mathbf{w}_2 + \omega_3 \mathbf{w}_3$ along the axis a_1 perpendicular to the pancake at $t = 6.89$. (b) Renormalized vorticity component $\omega_2/\omega_{\max}(t)$ vs. renormalized coordinate a_1/ℓ_1 at different times demonstrating self-similarity of the vorticity field.

is parallel to the pancake plane and is not orthogonal to the velocity. This indicates the importance of third dimension for the pancake dynamics.

The second simulation with the initial condition I_2 follows the same scenario for the global vorticity maximum and the associated region of high vorticity; see Appendix B. The corresponding characteristic times for the exponential behavior are estimated as $T_\omega \approx 2.7$, $T_\ell \approx 1.7$ and $T_\delta \approx 1.7$. Again, the two time scales $T_\delta \approx T_\ell$ are close, while the scale T_ω is considerably larger. We conclude that the pancake behavior is governed by the two characteristic times controlling the exponential growth of vorticity and the exponential decrease of pancake thickness.

IV. LOCAL MAXIMUMS OF VORTICITY

Figure 2(a) shows the vorticity distribution for the cross-section passing through the global maximum at final time. One can see that the regions of increased vorticity have a tendency to form a number of (thin and wide) pancake structures, which is in agreement with earlier simulations for generic initial conditions [35]. We expect that the structural analysis of these pancakes might give insight into the 3D Euler dynamics. However, direct identification of the pancakes is a complicated numerical problem. We approach this problem by finding and analyzing local maximums of the vorticity modulus, as described in Section II B.
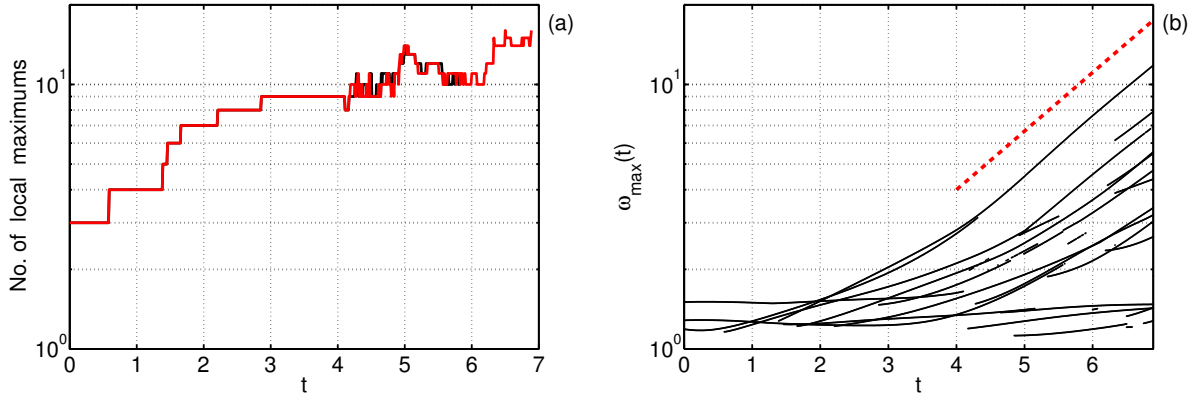
FIG. 7: *(Color on-line)* (a) Total number of local vorticity maximums versus time obtained for the two simulations corresponding to the total number of nodes $N_x N_y N_z \le 512^3$ (black, ends at $t = 5.83$) and 1024^3 (red). (b) Evolution of local vorticity maximums (logarithmic vertical scale). The dashed red line indicates the exponential slope $\propto e^{t/T_\omega}$ with characteristic time $T_\omega = 2$.

Figure 7(a) shows that the number of local maximums increases with time, from 3 at $t = 0$ to 16 at the end of the simulation. The values of vorticity modulus at maximum points are shown in Fig. 7(b). The results suggest that the vorticity growth tends to be exponential, $\omega_{\mathrm{max}}(t) \propto e^{t/T_\omega}$, for many of the local maximums with rather close values of the characteristic times T_ω.

Figure 8(a) shows the evolution of the three length scales, ℓ_1, ℓ_2 and ℓ_3, computed for each local maximum according to Eq. (9). We see that the smallest scale ℓ_1 (black) decays nearly exponentially, $\ell_1 \propto e^{-t/T_\ell}$, with rather close values of the characteristic time T_ℓ for different local maximums, while the scales ℓ_2 (blue) and ℓ_3 (red) remain the same or decrease slightly; recall that the large numerical error for the computation of ℓ_3 is related to the ill-conditioned Hessian matrix. This figure confirms the visual observation (Fig. 2) that most of the regions of increased vorticity tend to have the pancake shape characterized by the small spatial scale (thickness) ℓ_1 exponentially decreasing with time.

It is very instructive to see the distribution of local maximums among the spatial scales at fixed time, which highlights the contribution of different pancake structures to the energy at different scales. Using the estimate (15), we plot in Fig. 8(b) the characteristic wavenumbers k_1 for local maximums in decreasing order. The results suggest that the two leading maximums propagate much faster towards large wavenumbers. However, all the
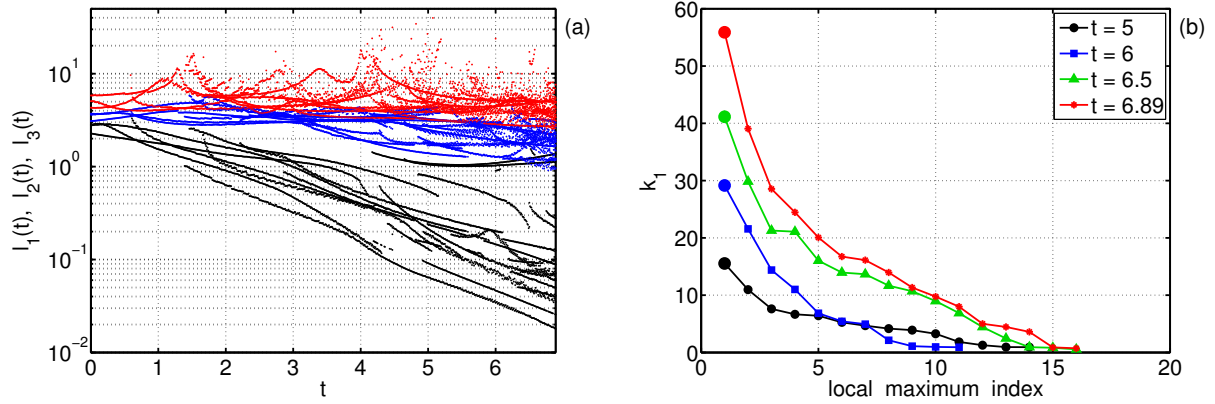
FIG. 8: *(Color on-line)* (a) Evolution of characteristic spatial scales ℓ_1 (black), ℓ_2 (blue) and ℓ_3 (red) of local maximums, see Eq. (9). Exponentially decreasing values of ℓ_1 indicate formation of the pancake structures in the vorticity field. (b) Characteristic wavenumbers k_1 estimated by Eq. (15) for the local maximums versus local maximum index numbers at different times. Local maximums are sorted in decreasing order of k_1. Large circles mark the global maximums.

other local maximums (i.e., most of the pancake structures) fill densely the interval from large to medium scales. Throughout this interval the distribution of maximums has a well-established slope (i.e., the pancakes are distributed with a specific "spectral density"). This interval increases with time and reaches $0 < k_1 \lesssim 30$ at the final time $t = 6.89$.

V. VORTICITY STRUCTURES AND THE KOLMOGOROV SPECTRUM

In fully developed turbulent flow with large Reynolds numbers, the energy from large scales is transported through a wide range of medium scales (the inertial interval) to small scales, where it is eventually dissipated, see [9–12]. The viscosity is negligible in the inertial interval, where the evolution can be described by the Euler equations. The dimensional considerations suggest the well-known Kolmogorov scaling law, $E_k \propto k^{-5/3}$, for the energy spectrum in the inertial interval. Our simulations can be seen as describing the initial stage of turbulent dynamics, developing from large-scale initial data, at times before the flow gets excited at viscous scales. Generally speaking, considerations of the Kolmogorov theory do not extend to this case, because the energy cascade is not formed yet. Thus, the scaling law $E_k \propto k^{-5/3}$ is not necessarily satisfied. From this point of view, our simulations of the 3D Euler equations give the possibility for studying the initial stage in formation of the
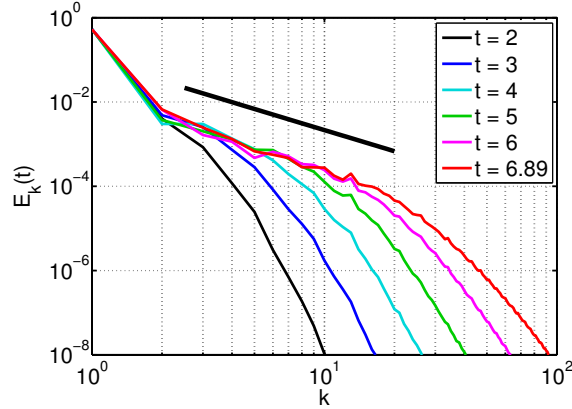
FIG. 9: *(Color on-line)* Energy spectrum $E_k(t)$ at different times. Straight line above the curves indicates the slope of the Kolmogorov power-law, $E_k \propto k^{-5/3}$.

Kolmogorov spectrum together with the respective energy transfer mechanisms.

Figure 9 shows that, at sufficiently small wavenumbers, we clearly observe the gradual formation of the Kolmogorov interval $E_k \propto k^{-5/3}$. This interval grows with time and extends to a decade of wavenumbers, $2 \lesssim k \lesssim 20$, at the end of the simulation. The Kolmogorov interval corresponds to the "frozen" part of the energy spectrum: $E_k(t)$ changes slightly with time in the Kolmogorov region in contrast to the vast changes at larger wavenumbers. Taking into account the times and logarithmic scale in Figure 9, one can guess that the size of the Kolmogorov interval increases exponentially in time.

In order to link the energy spectrum E_k with the pancake vorticity structures studied in the previous Sections, we look at the flow in Fourier space. One can expect that each pancake generates a structure extended in one direction in Fourier space ("jet"), aligned with the eigenvector $\mathbf{w}_1$ perpendicular to the pancake (such jets form, e.g., in the two-dimensional inviscid flow [54, 55]). Inside such a jet, the Fourier components of the flow should be large in comparison with the remaining background. In order to visualize this effect, we consider the function

$$\tilde{\boldsymbol{\omega}}(\mathbf{k}) = \boldsymbol{\omega}(\mathbf{k}) \Big/ \max_{|\mathbf{p}|=k} |\boldsymbol{\omega}(\mathbf{p})|, \qquad (16)$$

representing the Fourier transformed vorticity $\boldsymbol{\omega}(\mathbf{k})$ scaled to the maximal norm within each spherical shell. The reason for such a normalization is to compensate the strong decay of vorticity with k. Numerically, the maximum in Eq. (16) is computed among the nodes in a spherical shell of unit thickness.
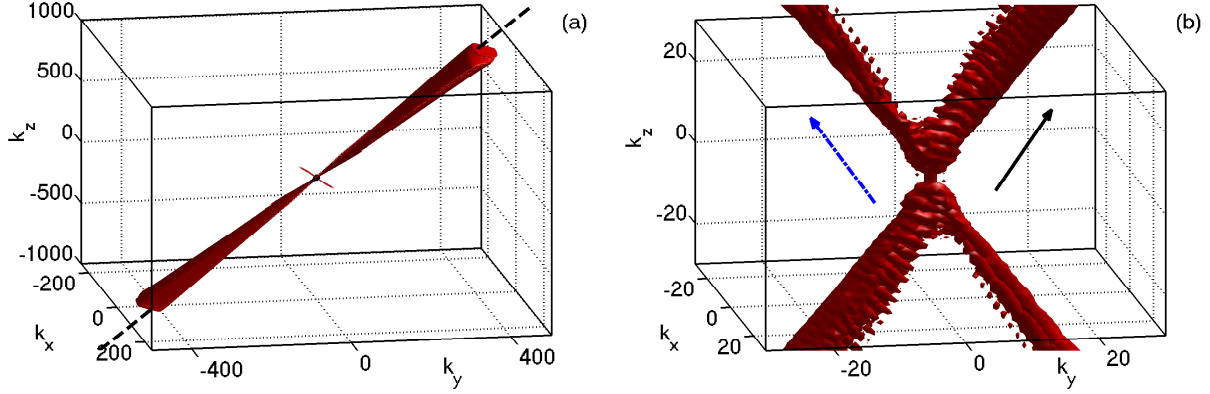
FIG. 10: *(Color on-line)* Isosurface $|\tilde{\boldsymbol{\omega}}(\mathbf{k})| = 0.2$ of the normalized vorticity field (16) in Fourier space at final time $t = 6.89$. (a) The jet is aligned with the eigenvector $\mathbf{w}_1$ (dashed black line), which is the normal direction of the pancake structure at the global vorticity maximum in physical space. (b) The closer view with the eigenvector $\mathbf{w}_1$ (solid black arrow) for the global vorticity maximum and the respective eigenvector (dash-dot blue arrow) for the third largest local maximum.

Figure 10(a) shows the isosurface $|\tilde{\boldsymbol{\omega}}(\mathbf{k})| = 0.2$, where the very thin interior part corresponds to larger vorticity, $|\tilde{\boldsymbol{\omega}}(\mathbf{k})| > 0.2$. As expected, this isosurface is aligned with the eigenvector $\mathbf{w}_1$ computed at the global maximum, which should bring the dominant contribution to Fourier components of vorticity at large k. Figure 10(b) demonstrates that the isosurface geometry is different at smaller wavenumbers, $k \lesssim 20$, corresponding to the Kolmogorov interval in Fig. 9. Here, different jets contribute and some of these jets can be clearly related to the pancakes of other local vorticity maximums (the figure shows directions for the first and third largest local maximums, while the second local maximum yields the direction very close to that for the first one). As shown in Fig. 11(a), the small interior part of this isosurface dominates in the energy spectrum. These observations reflect the extreme anisotropy of vorticity field and suggest that the Kolmogorov energy spectrum for $k \lesssim 20$ may be related to a collection of the pancake structures, rather than being determined solely by the dominant one. To further test this supposition, we integrate the energy spectrum inside each of the two jets $|\tilde{\boldsymbol{\omega}}(\mathbf{k})| > 0.2$ shown in Fig. 10(b), which can be separated from each other by cones of angle $\phi/2$, drawn from the origin around the corresponding eigenvectors $\mathbf{w}_1$. Here $\phi \approx \pi/4$ is the angle between the directions of the jets. One can see from Fig. 11(b) that the contributions of the jets to the energy spectrum are comparable at sufficiently small
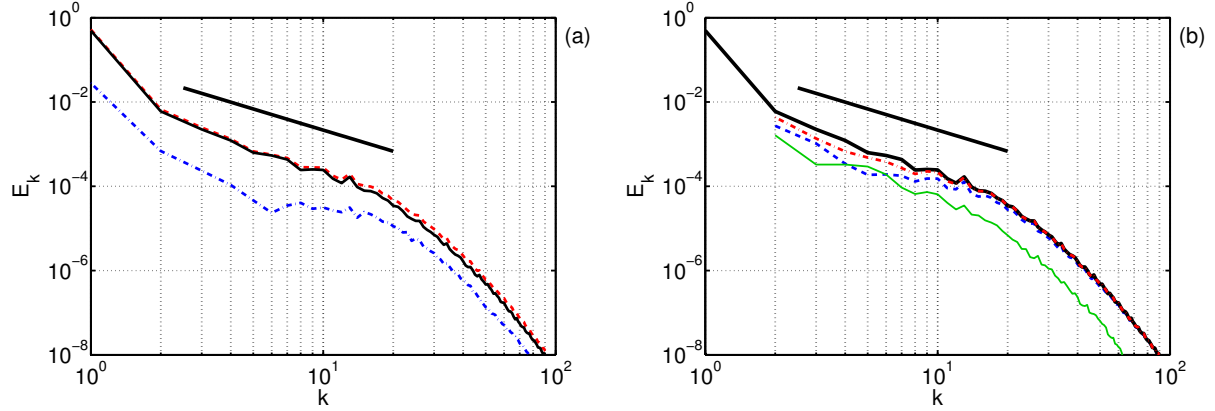
FIG. 11: *(Color on-line)* Energy spectrum E_k at the end of the simulation. (a) Calculated inside the isosurface $|\tilde{\boldsymbol{\omega}}(\mathbf{k})| > 0.2$ (solid black), outside this isosurface (dash-dot blue) and the sum of the two (dashed red). (b) Calculated inside the isosurface $|\tilde{\boldsymbol{\omega}}(\mathbf{k})| > 0.2$ (thick solid black), inside the first jet (dashed blue), inside the second jet (thin solid green), and the sum of the two jets (dash-dot red). Black line above the curves indicates the slope of the Kolmogorov power-law, $E_k \propto k^{-5/3}$.

wavenumbers in the Kolmogorov region, while at larger wavenumbers (both inside and outside the Kolmogorov region) the contribution from the leading jet becomes dominant. Thus, the energy spectrum at sufficiently large wavenumbers $k \gtrsim 20$ is determined mainly by the leading pancake structure corresponding to the global vorticity maximum. This means that the process of energy transfer to small scales is performed through the evolution of the pancake vorticity structures in the physical space. This interpretation is similar, in a spirit, to the simplified turbulence models [56] based, e.g., on Lundgren vortices [57, 58]. Note, however, that our simulation describes the initial stage of turbulence formation, when basic assumptions of these models related to stationary developed turbulence do not apply.

Statistical properties of the pancakes analyzed in the previous Section can be elaborated further in relation to Kolmogorov theory. Notice that the Kolmogorov interval in Fig. 9 approximately coincides with the interval of wavenumbers in Fig. 8(b) occupied by most of the pancake structures (except for the few largest local maximums with considerably larger wavenumbers). The Kolmogorov theory suggests the power-law $\langle |\delta v| \rangle \propto \ell^{1/3}$ for the mean velocity variation at spatial scales ℓ in the inertial interval, see e.g. [11, 12]. Similarly, it implies $\langle |\delta \omega| \rangle \propto \ell^{-2/3}$ for the vorticity variation. One can guess that the last relation is mainly determined by the small-scale high vorticity regions. In our simulations, that can
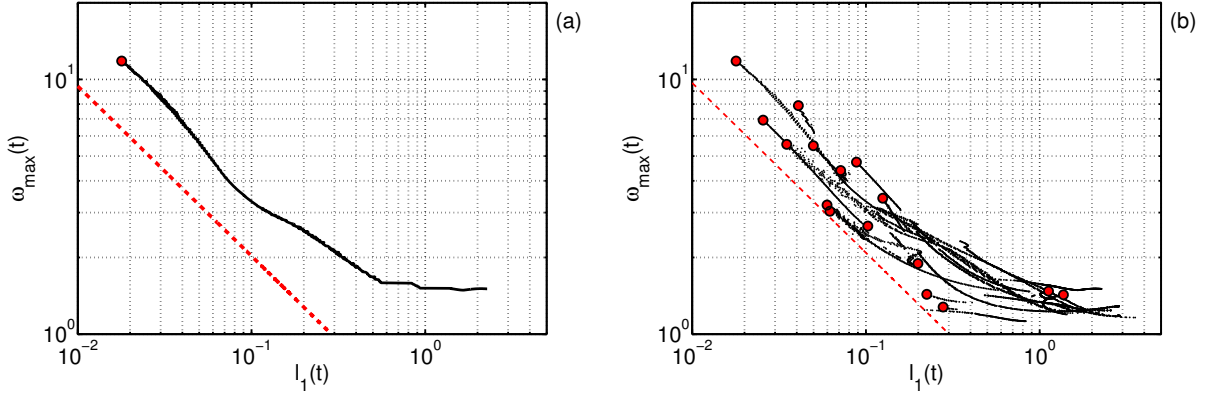
FIG. 12: *(Color on-line)* Relation between the vorticity local maximums $\omega_{\max}(t)$ and the respective characteristic lengths $\ell_1(t)$ during the evolution of the pancake structures: (a) for the global maximum, (b) for all local maximums. Red circles mark the local maximums at the final time $t = 6.89$. Dashed lines indicate the power-law $\omega_{\max} \propto \ell_1^{-2/3}$ in Eq. (17).

be seen as describing the initial stage of turbulent dynamics, these high vorticity regions appear in the form of the pancake structures. As we argued in the previous Section, each pancake is characterized by the spatial scale $\ell_1(t) \propto e^{-t/T_\ell}$ (the other two scales ℓ_2 and ℓ_3 remain close to 1) and the vorticity variation near the pancake is $|\delta\omega| \sim \omega_{\max}(t) \propto e^{t/T_\omega}$. Thus, we can test whether relation

$$\omega_{\max}(t) \propto \ell_1(t)^{-2/3}, \tag{17}$$

holds during the evolution of the pancake structures.

As shown in Fig. 12(a), the global vorticity maximum indeed evolves along the $\ell_1^{-2/3}$ law. This can be checked additionally by the ratio of the characteristic times T_ℓ and T_ω, that, according to relation (17), should be equal to $T_\ell/T_\omega = 2/3$. Our simulation provides the close relation $T_\ell/T_\omega \approx 0.7$ for the global vorticity maximum. It is also close for the simulation of the second initial condition I_2, which yields $T_\ell/T_\omega \approx 0.63$, see Appendix B. As one can see from Fig. 12(b), where the values of $\omega_{\max}$ are plotted versus the characteristic lengths ℓ_1 for all the local maximums, most local maximums have the tendency to follow the power law (17) asymptotically. Note that the observed behavior agrees with the asymptotic pancake dynamics in accordance with Eqs. (13)-(14). However, this model allows any value for the ratio T_ℓ/T_ω. The blowup scenario based on the vortex lines breaking [26, 59] leads to the 2/3 ratio for the pancake structure T_ℓ/T_ω and, thus, it can be considered as a possible

theoretical justification if extended to the case of the exponential vorticity growth. It is remarkable that local maximums follow approximately the same scaling law (17), with some shared constant prefactor before $\ell_1^{-2/3}$, and also that all local maximums taken at fixed time are distributed around this law, see red points in Fig. 12(b). These two properties indicate strong correlation of pancakes in the process of energy transport to small scales at initial stages of turbulent flow.

VI. CONCLUSIONS

In this work we performed the systematic numerical study of high vorticity structures that develop in the 3D incompressible Euler equations from smooth initial conditions of finite energy. Being motivated by the open problem of the finite-time blowup and its role for the developed turbulence, we are led to two important observations. First, we show that the exponential growth of vorticity, which is typically observed within pancakes (thin and wide vortex sheets), is compatible with the formation of Kolmogorov turbulent spectra in the fully inviscid flow, i.e., before the viscous scales get excited. Second, we show that the pancake structures, which have self-similar dynamics and develop in increasing number, play the crucial role in formation of the energy cascade to small scales.

We demonstrated that the thickness of pancake-like regions of high vorticity decreases exponentially in time, $\ell_1(t) \propto e^{-t/T_\ell}$, while the other two dimensions do not change considerably, $\ell_2 \sim \ell_3 \sim 1$. At the same time the local vorticity maximum grows exponentially, $\omega_{\max}(t) \propto e^{t/T_\omega}$. During the evolution, the relation $\omega_{\max}(t) \propto \ell_1(t)^{-2/3}$ resembling the Kolmogorov scaling law holds approximately in agreement with the ratio $T_\ell/T_\omega \approx 2/3$ between the characteristic times of the pancake compression T_ℓ and the vorticity growth T_ω. Since the pancake evolution is governed by the two different time scales T_ℓ and T_ω, this behavior does not agree with the pancake model (11) proposed in [35]. However, the modified model (13)-(14) satisfies the Euler equations for the leading terms and adequately describes the observed dynamics. The total number of pancake structures, estimated by the number of local vorticity maximums, increases with time. We demonstrate that at late times most of the pancakes are distributed densely across the corresponding interval of wavenumbers.

We clearly observe the formation of the Kolmogorov energy spectrum $E_k \propto k^{-5/3}$ in the inviscid system, together with the exponential (i.e., no finite-time blowup) vorticity

growth. The interval with Kolmogorov scaling grows with time and extends to a decade of wavenumbers at the end of the simulations. The energy spectrum $E_k(t)$ changes weakly with time in this region in contrast to vast changes at larger wavenumbers.

Thin pancake structures in physical space generate strongly anisotropic vorticity field in Fourier space in the form of "jets", which are extended in the directions perpendicular to the pancakes. Within these jets the Fourier components of the flow are large in comparison with the remaining background. We demonstrate that these jets occupy a small fraction of the entire spectral band, but provide the leading contribution to the energy spectrum of the system. This means that the energy transfer to small scales is performed through the evolution of the pancake structures, and that the Kolmogorov energy spectrum may be attributed to collective behavior of the pancakes.

Appendix A: Initial conditions

TABLE I: Nonzero coefficients in Eq. (6) for the initial vorticity field I_1 with the average energy density $E/(2\pi)^3 \approx 0.54$ and the average helicity density $\Omega/(2\pi)^3 \approx 1.05$. Final time for this simulation is $t = 6.89$ and the final grid is $486 \times 1024 \times 2048$. The simulation is affected by aliasing starting from $t \approx 5.13$.

h	$\mathbf{A_h}$	$\mathbf{B_h}$
(-1,0,2)	(0.0065641, 0.0027931, 0.003282)	(0.0044136, 0.0056271, 0.0022068)
(0,0,0)	(0.065101, 0.0005801, -0.064109)	(0.0045744, -0.022895, 0.18392)
(0,0,1)	(0, 1, 0)	(1, 0, 0)
(0,0,2)	(0, 0.01, 0)	(0.01, 0, 0)
(0,1,0)	(0.21204, 0, -0.070625)	(-0.14438, 0, 0.23298)
(0,1,1)	(0.045977, -0.010151, 0.010151)	(0.041942, 0.040326, -0.040326)
(0,2,0)	(0.005, 0, 0)	(0, 0, 0.005)
(1,0,0)	(0, 0, 0.1)	(0, 0.1, 0)
(1,0,1)	(-0.046112, 0.017081, 0.046112)	(-0.0097784, 0.020122, 0.0097784)
(1,1,2)	(-0.0034664, 0.0049556, -0.00074462)	(-0.0059316, -0.0010472, 0.0034894)
(2,0,0)	(0, 0, 0.02)	(0, 0.02, 0)

TABLE II: Nonzero coefficients in Eq. (6) for the initial vorticity field I_2 with the average energy density $E/(2\pi)^3 \approx 0.51$ and the average helicity density $\Omega/(2\pi)^3 \approx 1$. Final time for this simulation is $t = 7.77$ and the final grid is $1152 \times 384 \times 2304$. The simulation is affected by aliasing starting from $t \approx 6.25$.

h	$\mathbf{A_h}$	$\mathbf{B_h}$
(-1,0,1)	(-0.040618, 0.039651, -0.040618)	(-0.030318, 0.064657, -0.030318)
(0,0,0)	(0.067751, -0.1311, -0.11256)	(-0.082614, -0.0364, 0.18932)
(0,0,1)	(0, 1, 0)	(1, 0, 0)
(0,1,1)	(0.0062549, 0.044315, -0.044315)	(0.034983, -0.014521, 0.014521)
(1,0,0)	(0, 0.079395, 0.07027)	(0, 0.099411, 0.012762)
(1,1,0)	(-0.047174, 0.047174, -0.045572)	(-0.049622, 0.049622, 0.001773)

Appendix B: Simulation results for the initial condition I_2

In this Appendix we provide some results for the simulation with initial condition I_2, which reaches the time $t = 7.77$ on the grid $1152 \times 384 \times 2304$. The region of global vorticity maximum represents at final time a very thin pancake structure, as shown in Fig. 13 by the numerically computed isosurface $|\boldsymbol{\omega}(\mathbf{r})| = 0.8\,\omega_{\max}$ in the local coordinates (a_1, a_2, a_3), see Eq. (9). The number of local maximums increases with time, from 2 at $t = 0$ to 13 at the end of the simulation. The values of vorticity modulus at maximum points tend to grow exponentially in time, $\omega_{\max}(t) \propto e^{t/T_\omega}$, with different but relatively close values of the characteristic times T_ω, Fig. 14(a). The thickness of the associated high vorticity regions decays nearly exponentially, $\ell_1(t) \propto e^{-t/T_\ell}$, while the other two scales ℓ_2 and ℓ_3 remain the same or decrease slightly in time, Fig. 14(b).

The gradual formation of the Kolmogorov region $E_k \propto k^{-5/3}$ in the energy spectrum is shown in Fig. 15(a). This region extends to $5 \lesssim k \lesssim 15$ at the end of the simulation, and corresponds to the "frozen" part of the spectrum where $E_k(t)$ changes slightly in time, in contrast to the vast changes at larger wavenumbers. The size of this interval is smaller than for the first simulation in Fig. 9, but the same tendency is clearly observed. Fig. 15(b) shows the characteristic wavenumbers $k_1 = 1/\ell_1$ for local maximums in decreasing order. The first three local maximums propagate much faster to higher wavenumbers, while the other local maximums fill densely the interval from large to medium scales, which approximately coincides with the Kolmogorov region in the energy spectrum.

Fig. 16(a) shows the isosurface of renormalized Fourier components of vorticity $|\tilde{\boldsymbol{\omega}}(\mathbf{k})| = 0.2$, see Eq. (16), where the very thin interior part corresponds to larger vorticity. This isosurface is aligned close to the eigenvector $\mathbf{w}_1$ computed at the global vorticity maximum. At smaller wavenumbers $k \lesssim 15$, corresponding to the Kolmogorov interval in Fig. 15(a), the isosurface represents a union of several jets, Fig. 16(b), that are clearly related to other local vorticity maximums (the figure shows the directions of the first, second and fourth largest local maximums, while the third local maximum yields the direction very close to that for the first one). The small interior part of the isosurface $|\tilde{\boldsymbol{\omega}}(\mathbf{k})| = 0.2$ dominates in the energy spectrum, Fig. 17(a). The contributions of the jets to the energy spectrum are comparable at sufficiently small wavenumbers from the Kolmogorov region, while at larger wavenumbers (both inside and outside the Kolmogorov region) the contribution from the

leading jet becomes dominant, Fig. 17(b). As shown in Fig. 18, vorticity maximums tend to evolve along the $\omega_{\max}(t) \propto \ell_1(t)^{-2/3}$ power-law, with rather close values of the constant prefactors before $\ell_1^{-2/3}$ for most of them. Thus, the simulation for the second initial condition leads to the same conclusions on the formation and structure of the Kolmogorov turbulent spectrum, as deduced for the first simulation in the main text of the paper.
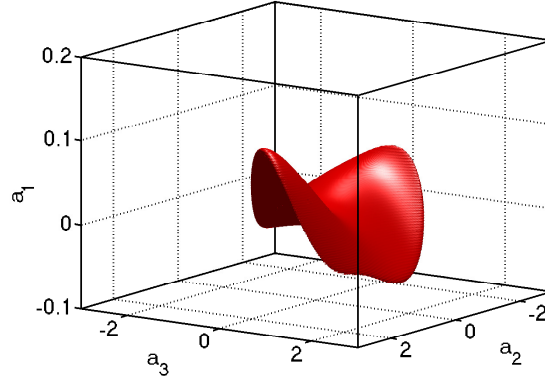

FIG. 13: *(Color on-line)* Isosurface of constant vorticity $|\boldsymbol{\omega}| = 0.8\,\omega_{\max}$ in the local coordinates (a_1, a_2, a_3) at the final time of the simulation, $t = 7.77$. Note much smaller vertical scale.
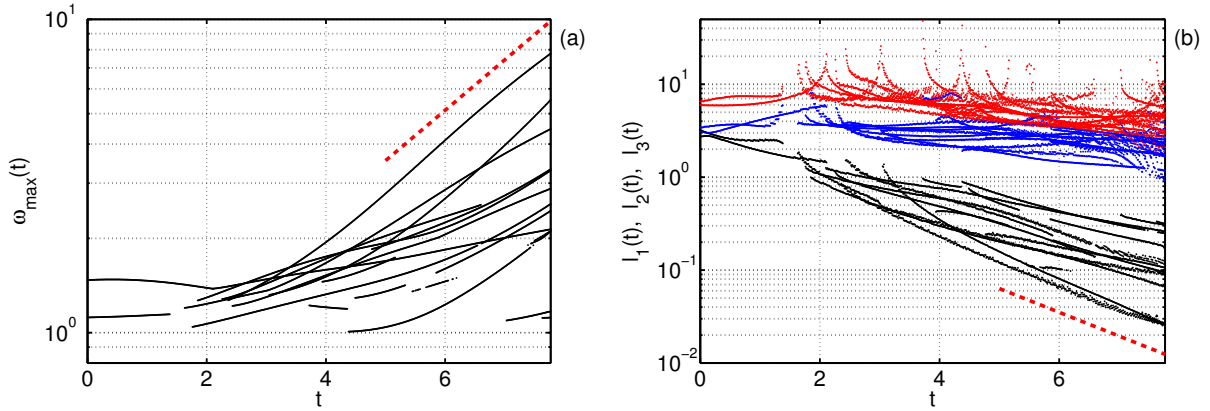

FIG. 14: *(Color on-line)* (a) Evolution of local vorticity maximums (logarithmic vertical scale). The dashed red line indicates the exponential slope $\propto e^{t/T_\omega}$ with characteristic time $T_\omega = 2.7$. (b) Evolution of characteristic spatial scales ℓ_1 (black), ℓ_2 (blue) and ℓ_3 (red) of local maximums, see Eq. (9). The dashed red line indicates the exponential slope $\propto e^{-t/T_\ell}$ with characteristic time $T_\ell = 1.7$.
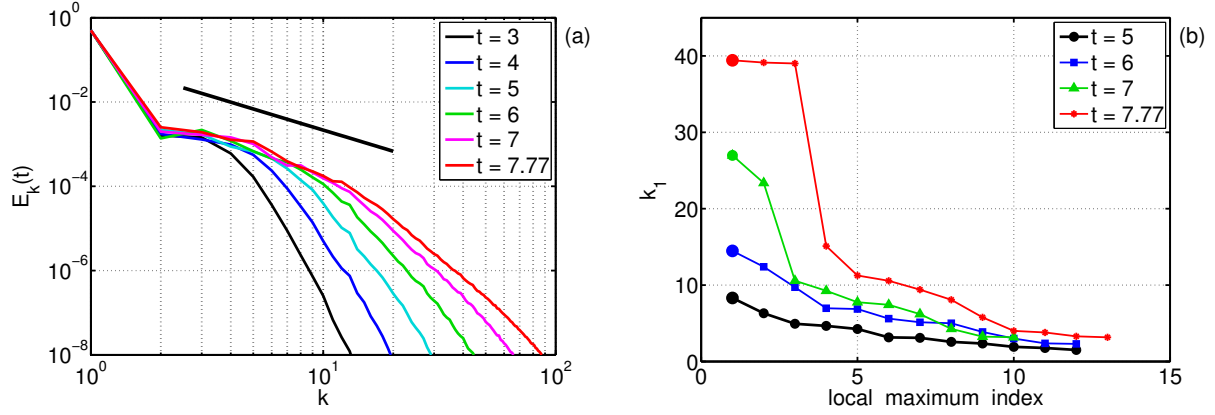
FIG. 15: *(Color on-line)* (a) Energy spectrum $E_k(t)$ at different times. Straight line above the curves indicates the slope of the Kolmogorov power-law, $E_k \propto k^{-5/3}$. (b) Characteristic wavenumbers k_1 estimated by Eq. (15) for the local maximums versus local maximum index numbers at different times. Local maximums are sorted in decreasing order of k_1. Large circles mark the global maximums.
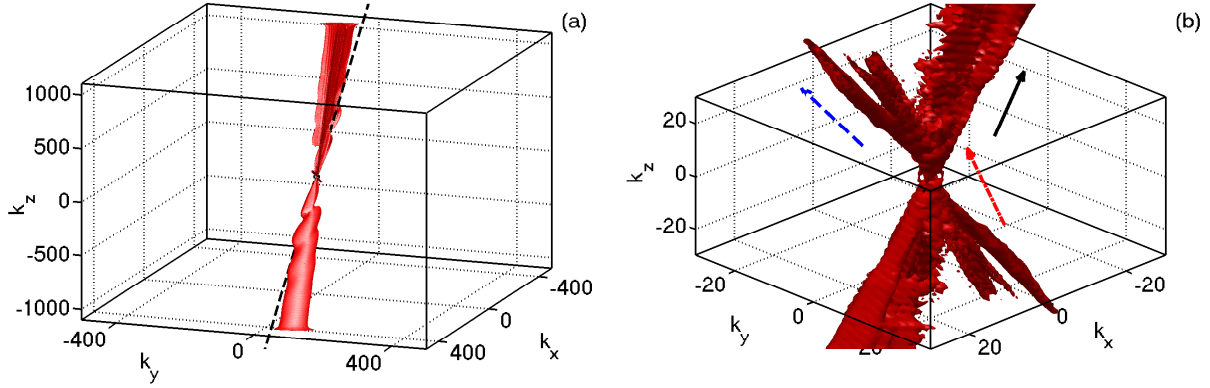

FIG. 16: *(Color on-line)* Isosurface $|\tilde{\boldsymbol{\omega}}(\mathbf{k})| = 0.2$ of the normalized vorticity field (16) in Fourier space at final time $t = 7.77$. (a) The jet is aligned with the eigenvector $\mathbf{w}_1$ (dashed black line), which is the normal direction of the pancake structure at the global vorticity maximum in physical space. (b) The closer view with the eigenvector $\mathbf{w}_1$ (solid black arrow) for the global vorticity maximum and the similar eigenvectors for the second (dashed blue arrow) and the fourth (dash-dot red arrow) largest local maximums.
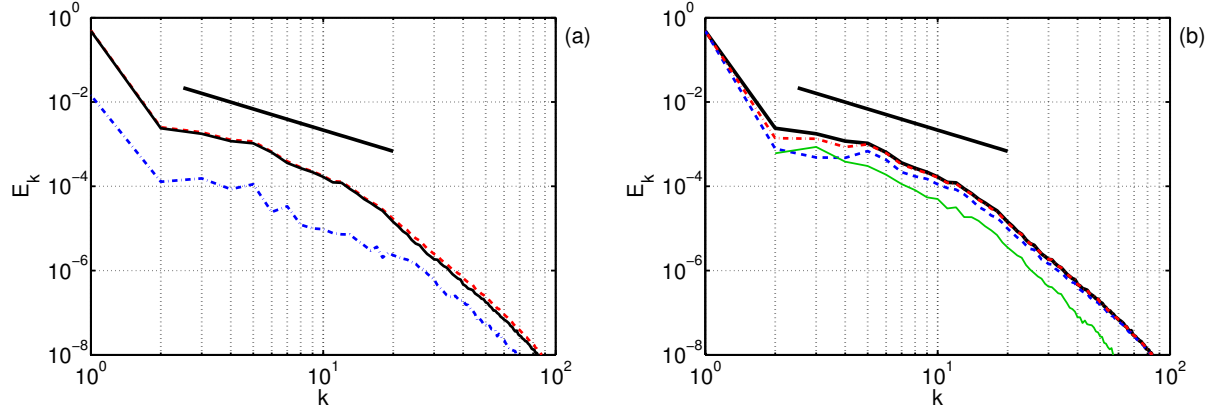
FIG. 17: *(Color on-line)* Energy spectrum E_k at the end of the simulation. (a) Calculated inside the isosurface $|\tilde{\boldsymbol{\omega}}(\mathbf{k})| > 0.2$ (solid black), outside this isosurface (dash-dot blue) and the sum of the two (dashed red). (b) Calculated inside the isosurface $|\tilde{\boldsymbol{\omega}}(\mathbf{k})| > 0.2$ (thick solid black), inside the first jet (dashed blue), inside the second and third jets (thin solid green), and the sum of the three jets (dash-dot red). Black line above the curves indicates the slope of the Kolmogorov power-law, $E_k \propto k^{-5/3}$.
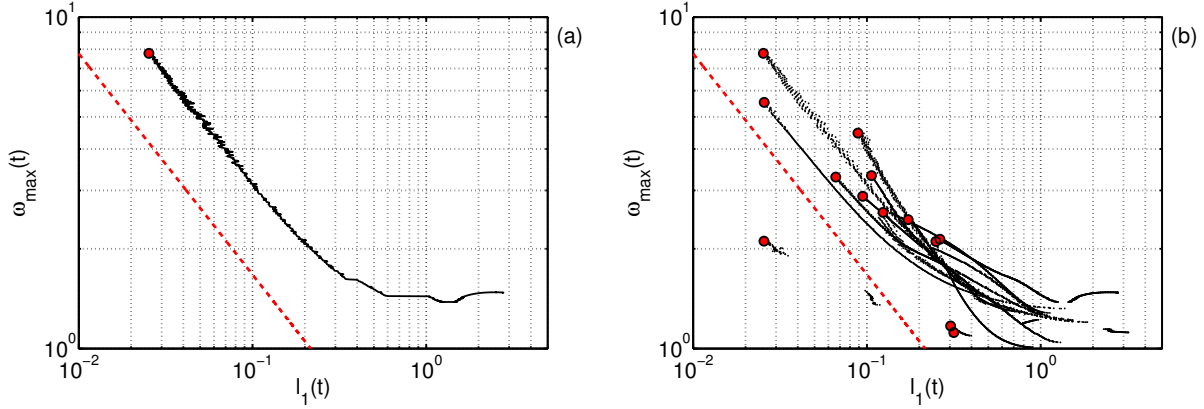

FIG. 18: *(Color on-line)* Relation between the vorticity local maximums $\omega_{\max}(t)$ and the respective characteristic lengths $\ell_1(t)$ during the evolution of the pancake structures: (a) for the global maximum, (b) for all local maximums. Red circles mark the local maximums at the final time $t = 7.77$. Dashed lines indicate the power-law $\omega_{\max} \propto \ell_1^{-2/3}$ in Eq. (17).

[1] J. Leray, "Sur le mouvement d'un liquide visqueux emplissant l'espace," *Acta Math.*, vol. 63, no. 1, pp. 193–248, 1934.

[2] L. Onsager, "Statistical hydrodynamics," *Nuovo Cimento*, vol. 6, pp. 279–287, 1949.

[3] P. G. Saffman, "Dynamics of vorticity," *J. Fluid Mech.*, vol. 106, pp. 49–58, 1981.

[4] P. Constantin, "On the Euler equations of incompressible fluids," *B. Am. Math. Soc.*, vol. 44, no. 4, pp. 603–622, 2007.

[5] J. D. Gibbon, M. Bustamante, and R. M. Kerr, "The three-dimensional Euler equations: singular or non-singular?," *Nonlinearity*, vol. 21, p. T123, 2008.

[6] O. M. Phillips, "The scattering of gravity waves by turbulence," *J. Fluid Mech.*, vol. 5, no. 2, pp. 177–192, 1959.

[7] K. Hasselmann, "Weak-interaction theory of ocean waves," *Basic Developments in Fluid Dynamics*, vol. 2, pp. 117–182, 1968.

[8] E. A. Kuznetsov, "Wave collapse in plasmas and fluids," *Chaos: An Interdisciplinary Journal of Nonlinear Science*, vol. 6, no. 3, pp. 381–390, 1996.

[9] A. N. Kolmogorov, "The local structure of turbulence in incompressible viscous fluid for very large Reynolds numbers," *Dokl. Akad. Nauk SSSR*, vol. 30, no. 4, pp. 299–303, 1941.

[10] A. M. Obukhov, "Spectral energy distribution in a turbulent flow," *Dokl. Akad. Nauk SSSR*, vol. 32, no. 1, pp. 22–24, 1941.

[11] L. Landau and E. Lifshitz, *Fluid Mechanics. Course of Theoretical Physics*, vol. 6. Elsevier, 2013.

[12] U. Frisch, *Turbulence: the legacy of A.N. Kolmogorov.* Cambridge University Press, 1999.

[13] A. A. Mailybaev, "Blowup as a driving mechanism of turbulence in shell models," *Physical Review E*, vol. 87, p. 053011, 2013.

[14] A. A. Mailybaev, "Computation of anomalous scaling exponents of turbulence from self-similar instanton dynamics," *Phys. Rev. E*, vol. 86, no. 2, p. 025301, 2012.

[15] P. Orlandi and S. Pirozzoli, "Vorticity dynamics in turbulence growth," *Theor. Comput. Fluid Dyn.*, vol. 24, pp. 247–251, 2010.

[16] D. D. Holm and R. M. Kerr, "Transient vortex events in the initial value problem for turbulence," *Phys. Rev. Lett.*, vol. 88, no. 24, p. 244501, 2002.

[17] D. D. Holm and R. M. Kerr, "Helicity in the formation of turbulence," *Physics of Fluids*, vol. 19, p. 025101, 2007.

[18] J. T. Beale, T. Kato, and A. Majda, "Remarks on the breakdown of smooth solutions for the 3-D Euler equations," *Communications in Mathematical Physics*, vol. 94, no. 1, pp. 61–66, 1984.

[19] P. Constantin, C. Fefferman, and A. J. Majda, "Geometric constraints on potentially singular solutions for the 3-D Euler equations," *Comm. Partial Differential Equations*, vol. 21, no. 3-4, pp. 559–571, 1996.

[20] J. Deng, T. Hou, and X. Yu, "Improved geometric conditions for non-blowup of the 3D incompressible Euler equation," *Comm. Partial Differential Equations*, vol. 31, no. 2, pp. 293–306, 2006.

[21] J. Deng, Y. H. Thomas, and X. Yu, "Geometric properties and nonblowup of 3D incompressible Euler flow," *Comm. Partial Differential Equations*, vol. 30, no. 1-2, pp. 225–243, 2005.

[22] D. Chae, "On the finite-time singularities of the 3D incompressible Euler equations," *Comm. Pure Appl. Math.*, vol. 60, no. 4, pp. 597–617, 2007.

[23] D. Chae, *Incompressible Euler Equations: the blow-up problem and related results. In: Handbook of Differential Equations: Evolutionary Equation (C.M. Dafermos and M. Pokorny, Eds.), Vol. 4*, pp. 1–55. Elsevier, 2008.

[24] T. Y. Hou, "Blow-up or no blow-up? A unified computational and analytic approach to 3D incompressible Euler and Navier–Stokes equations," *Acta Numerica*, vol. 18, pp. 277–346, 2009.

[25] J. D. Gibbon, "Dynamics of scaled norms of vorticity for the three-dimensional Navier-Stokes and Euler equations," *Procedia IUTAM*, vol. 7, pp. 39–48, 2013.

[26] E. A. Kuznetsov and V. P. Ruban, "Collapse of vortex lines in hydrodynamics," *Journal of Experimental and Theoretical Physics*, vol. 91, no. 4, pp. 775–785, 2000.

[27] E. A. Kuznetsov and A. V. Mikhailov, "On the topological meaning of canonical Clebsch variables," *Physics Letters A*, vol. 77, no. 1, pp. 37–38, 1980.

[28] J. M. Greene and O. N. Boratav, "Evidence for the development of singularities in Euler flow," *Physica D: Nonlinear Phenomena*, vol. 107, no. 1, pp. 57–68, 1997.

[29] J. M. Greene and R. B. Pelz, "Stability of postulated, self-similar, hydrodynamic blowup solutions," *Phys. Rev. E*, vol. 62, no. 6, p. 7982, 2000.

[30] A. A. Mailybaev, "Renormalization and universality of blowup in hydrodynamic flows," *Physical Review E*, vol. 85, no. 6, p. 066317, 2012.

[31] A. A. Mailybaev, "Renormalization group formalism for incompressible Euler equations and the blowup problem," *arXiv preprint arXiv:1203.3348*, 2012.

[32] J. D. Gibbon, "The three-dimensional Euler equations: Where do we stand?," *Phys. D*, vol. 237, no. 14-17, pp. 1894–1904, 2008.

[33] G. Luo and T. Y. Hou, "Potentially singular solutions of the 3D incompressible Euler equations," *arXiv preprint arXiv:1310.0497*, 2013.

[34] A. Larios and E. S. Titi, "Global regularity vs. finite-time singularities: Some paradigms on the effect of boundary conditions and certain perturbations," *arXiv preprint arXiv:1401.1534*, 2014.

[35] M. E. Brachet, M. Meneguzzi, A. Vincent, H. Politano, and P. L. Sulem, "Numerical evidence of smooth self-similar dynamics and possibility of subsequent collapse for three-dimensional ideal flows," *Phys. Fluids A*, vol. 4, pp. 2845–2854, 1992.

[36] A. Pumir and E. Siggia, "Collapsing solutions to the 3-D Euler equations," *Phys. Fluids A*, vol. 2, pp. 220–241, 1990.

[37] K. Ohkitani, "A geometrical study of 3D incompressible Euler flows with Clebsch potentialsa long-lived Euler flow and its power-law energy spectrum," *Physica D: Nonlinear Phenomena*, vol. 237, no. 14, pp. 2020–2027, 2008.

[38] R. M. Kerr, "Vortex collapse and turbulence," *Fluid Dynamics Research*, vol. 36, pp. 249–260, 2005.

[39] R. M. Kerr, "Evidence for a singularity of the three-dimensional, incompressible Euler equations," *Physics of Fluids A: Fluid Dynamics (1989-1993)*, vol. 5, no. 7, pp. 1725–1746, 1993.

[40] R. M. Kerr, "Velocity and scaling of collapsing Euler vortices," *Physics of Fluids*, vol. 17, no. 7, p. 075103, 2005.

[41] T. Y. Hou and R. Li, "Computing nearly singular solutions using pseudo-spectral methods," *J. Comp. Phys.*, vol. 226, no. 1, pp. 379–397, 2007.

[42] M. D. Bustamante and R. M. Kerr, "3D Euler about a 2D symmetry plane," *Physica D*, vol. 237, no. 14, pp. 1912–1920, 2008.

[43] R. M. Kerr, "Bounds for Euler from vorticity moments and line divergence," *Journal of Fluid Mechanics*, vol. 729, p. R2, 2013.

[44] R. Grauer, C. Marliani, and K. Germaschewski, "Adaptive mesh refinement for singular solutions of the incompressible Euler equations," *Physical review letters*, vol. 80, no. 19, p. 4177, 1998.

[45] P. Orlandi, S. Pirozzoli, and G. F. Carnevale, "Vortex events in Euler and Navier–Stokes simulations with smooth initial conditions," *Journal of Fluid Mechanics*, vol. 690, pp. 288–320, 2012.

[46] S. Kida, "Three-dimensional periodic flows with high-symmetry," *J. Phys. Soc. Japan*, vol. 54, pp. 2132–2136, 1985.

[47] O. N. Boratav and R. B. Pelz, "Direct numerical simulation of transition to turbulence from a high-symmetry initial condition," *Phys. Fluids*, vol. 6, pp. 2757–2784, 1994.

[48] R. B. Pelz, "Symmetry and the hydrodynamic blow-up problem," *Journal of Fluid Mechanics*, vol. 444, pp. 299–320, 2001.

[49] T. Grafke, H. Homann, J. Dreher, and R. Grauer, "Numerical simulations of possible finite time singularities in the incompressible Euler equations: comparison of numerical methods," *Physica D*, vol. 237, no. 14, pp. 1932–1936, 2008.

[50] T. Y. Hou and R. Li, "Blowup or no blowup? The interplay between theory and numerics," *Physica D*, vol. 237, no. 14, pp. 1937–1944, 2008.

[51] C. Cichowlas, P. Bonaïti, F. Debbasch, and M. Brachet, "Effective dissipation and turbulence in spectrally truncated Euler flows," *Physical review letters*, vol. 95, no. 26, p. 264502, 2005.

[52] E. A. Kuznetsov and V. P. Ruban, "Hamiltonian dynamics of vortex lines in hydrodynamic-type systems," *Journal of Experimental and Theoretical Physics Letters*, vol. 67, no. 12, pp. 1076–1081, 1998.

[53] E. A. Kuznetsov and V. P. Ruban, "Hamiltonian dynamics of vortex and magnetic lines in hydrodynamic type systems," *Physical Review E*, vol. 61, no. 1, pp. 831–841, 2000.

[54] E. A. Kuznetsov, V. Naulin, A. H. Nielsen, and J. J. Rasmussen, "Effects of sharp vorticity gradients in two-dimensional hydrodynamic turbulence," *Phys. Fluids*, vol. 19, no. 10, p. 105110, 2007.

[55] A. N. Kudryavtsev, E. A. Kuznetsov, and E. V. Sereshchenko, "Statistical properties of freely decaying two-dimensional hydrodynamic turbulence," *JETP Lett.*, vol. 96, no. 11, pp. 783–789, 2012.

[56] D. I. Pullin and P. G. Saffman, "Vortex dynamics in turbulence," *Annual review of fluid*

mechanics, vol. 30, no. 1, pp. 31–51, 1998.

[57] T. S. Lundgren, "Strained spiral vortex model for turbulent fine structure," *Physics of Fluids (1958-1988)*, vol. 25, no. 12, pp. 2193–2203, 1982.

[58] A. D. Gilbert, "A cascade interpretation of Lundgrens stretched spiral vortex model for turbulent fine structure," *Physics of Fluids A: Fluid Dynamics (1989-1993)*, vol. 5, no. 11, pp. 2831–2834, 1993.

[59] E. A. Kuznetsov, "Breaking of vortex and magnetic field lines in hydrodynamics and MHD," *Plasmas in the Laboratory and in the Universe: New Insights and New Challenges*, vol. 703, no. 1, pp. 16–25, 2004.